ACS NANO
Cite This: ACS Nano 2019, 13, 4455−4468
www.acsnano.org

ARTICLE

# Conformation Dependence of Diphenylalanine Self-Assembly Structures and Dynamics: Insights from Hybrid-Resolution Simulations

Qinsi Xiong,[†] Yixiang Jiang,[†] Xiang Cai, Fadeng Yang, Zigang Li,* and Wei Han*

State Key Laboratory of Chemical Oncogenomics, School of Chemical Biology and Biotechnology, Peking University Shenzhen Graduate School, Shenzhen 518055, China

Supporting Information

**ABSTRACT:** The molecular design of peptide-assembled nanostructures relies on extensive knowledge pertaining to the relationship between conformational features of peptide constituents and their behavior regarding self-assembly, and characterizing the conformational details of peptides during their self-assembly is experimentally challenging. Here, we demonstrate that a hybrid-resolution modeling method can be employed to investigate the role that conformation plays during the assembly of terminally capped diphenylalanines (FF) through microsecond simulations of hundreds or thousands of peptides. Our simulations discovered tubular or vesicular nanostructures that were consistent with experimental observation while reproducing critical self-assembly concentration and secondary structure contents in the assemblies that were measured in our experiments. The atomic details provided by our method allowed us to uncover diverse FF conformations and conformation dependence of assembled nanostructures. We found that the assembled morphologies and the molecular packing of FFs in the observed assemblies are linked closely with side-chain angle and peptide bond orientation, respectively. Of various conformations accessible to soluble FFs, only a select few are compatible with the assembled morphologies in water. A conformation resembling a FF crystal, in particular, became predominant due to its ability to permit highly ordered and energetically favorable FF packing in aqueous assemblies. Strikingly, several conformations incompatible with the assemblies arose transiently as intermediates, facilitating key steps of the assembly process. The molecular rationale behind the role of these intermediate conformations were further explained. Collectively, the structural details reported here advance the understanding of the FF self-assembly mechanism, and our method shows promise for studying peptide-assembled nanostructures and their rational design.

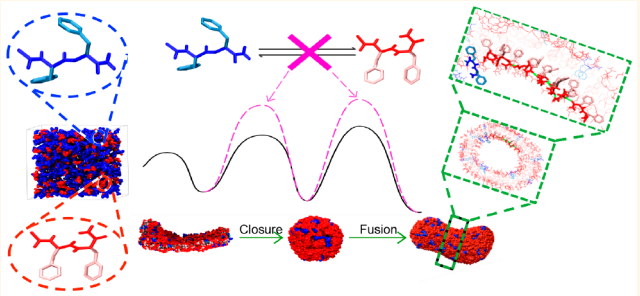


**KEYWORDS:** *diphenylalanine self-assembly, hybrid-resolution force field, molecular dynamic simulation, peptide nanotube, peptide secondary structure, conformational dynamics, flip-flop motion*

Peptide-assembled materials have garnered great attention in recent years due to their simplicity, availability, excellent biocompatibility, and biodegradability and have gradually aided in great achievements in material science.[1−5] Diphenylalanine (FF), derived originally from the core motif of disease-related amyloid-$\beta$ peptides, is one of the simplest molecules that can form these types of materials.[6] In water, FFs self-assemble into nanotubes, but other assembled structures such as nanospheres, nanofibers, nanowires, nanosheet, *etc.* are also attainable depending on assembly conditions and chemical modifications introduced.[6−14] Due to their excellent optoelectrical and mechanical properties, these FF-based materials have various applications ranging from batteries to tissue repair.[3,4,15,16]

A central task of the molecular design for FF-based materials is establishing the relationships between structures of constituent peptides and assembled supramolecular structures with the aim of applying these relationships to design materials with targeted assembled structures and properties.[17,18] When achieving this goal, it is necessary to elucidate molecular factors underlying the self-assembly process. The importance of

Received: December 26, 2018
Accepted: March 14, 2019
Published: March 14, 2019

Downloaded via PEKING UNIV on August 7, 2019 at 08:24:25 (UTC).
See https://pubs.acs.org/sharingguidelines for options on how to legitimately share published articles.


© 2019 American Chemical Society

DOI: 10.1021/acsnano.8b09741
ACS Nano 2019, 13, 4455−4468

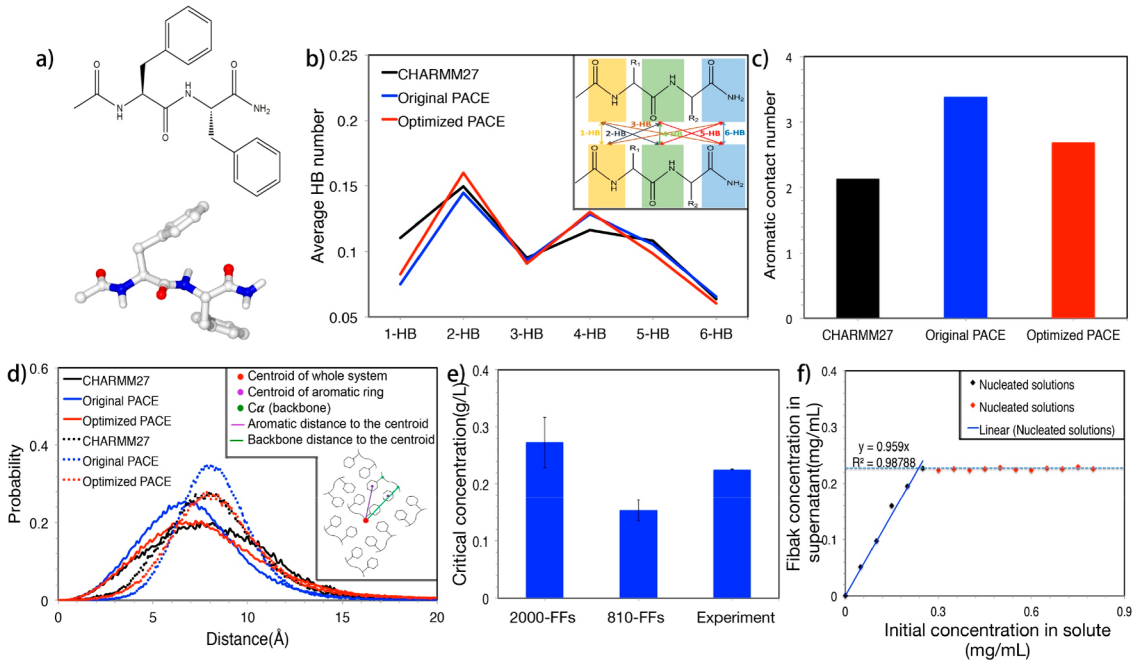


**Figure 1. (a) Chemical structure of FF and its representation using PACE. Color code: red for oxygen; gray for carbon; blue for nitrogen; white for hydrogen. (b) Average count of HBs formed between any two FFs calculated according to simulations of a 8 FF system using all-atom models (black) and original (blue) and optimized PACE (red). HB contacts were analyzed for each possible pair of peptide bonds from any two FFs (see the inset). A HB between two peptide bonds was thought to arise if the donor−acceptor distance is shorter than 0.35 nm and the donor−hydrogen−acceptor angle is greater than 120°. (c) Average aromatic contacts involved with each aromatic side chain. Two aromatic rings form a contact if their centroid distance is shorter than 0.65 nm. (d) Distributions of distance of aromatic side chains (solid curves) or $C_\alpha$ atoms (dotted curves) to the centroid of the 8 FF system. The inset illustrates the definitions of these distances. (e) Critical concentration of FF self-assembly obtained from the simulations and the absorbance experiment. Error bars of the simulated results were obtained as block average by dividing the last one-third of the simulations. (f) Supernatant concentration of FFs measured at 330 K as a function of initial concentrations of FFs added.**

noncovalent forces between peptide molecules is evident. The knowledge regarding the roles of these forces in the self-assembly of FF-based molecules have been greatly advanced thanks to numerous insightful experimental studies and simulations.[19−29] However, one of the main hurdles that prevent further understanding of the self-assembly process lies in the conformational flexibility inherent to FF peptides.[30,31]

There have been many reported examples of various secondary structures in FF-based assemblies, including $\beta$-sheets, $\alpha$-helices, and turns when exposed to distinct external conditions in pH, temperature, and solvent environment.[7,13,32,33] Although the exact nature of the corresponding conformations of FF building blocks remains unknown, it is conceivable that there could be many diverse peptide backbone conformations. Different conformations may exhibit distinct side-chain arrangements and hydrogen bond donor and acceptor orientations for backbone. These local geometric features dictate how the building blocks may interact with their neighbors, which can sometimes result in a long-range structural order and allow for particular supramolecular structure formation.[31,34−38] It is important, therefore, to explore internal conformations accessible to FF-based building blocks and investigate the conformational dependence of molecular packing and supramolecular structures.

The diverse conformations present in FF-based molecules further imply that these molecules would undergo conformational changes when exposed to thermal forces, thereby altering the way they would interact with their surroundings. Presented in a recent kinetic study using Raman spectroscopy, heterogeneous conformational transitions of FFs were indeed observed during their self-assembly into nanotubes.[39] In general, conformational fluctuation of protein-like molecules can be crucial for self-assembly processes.[40] It has been suggested that a reconfiguration of protein-like building blocks may assist systems in escaping trapped states, thereby facilitating either the formation of correctly assembled structures or the transformation of assemblies between different structures.[41,42] The role of conformational fluctuation in the assembly process of FF-based systems, however, still awaits elucidation.

Characterizing peptide conformations in assemblies remains challenging. Methods that rely on ensemble average such as infrared absorption, circular dichroism, and X-ray diffraction oftentimes cannot resolve conformations of individual amino acids.[17] X-ray crystallography has been applied in resolving atomic structures of FF-based molecules,[43,44] but it is still unclear if crystallized molecules assume the exact same conformation as they do in the assembly.[45,46]

Molecular dynamics simulations have provided another means of investigating molecular details of FF self-assembly.[22,24,25,28,29,47−50] All-atom simulations, although arguably accurate, usually can examine the self-assembly of only a small number of peptide molecules in relatively short time scales. FF-based molecular conformations were typically examined at a monomer level[47] or in small self-assembled structures that were composed of dozens of peptide molecules.[24,25,48] Alternatively, coarse-grained (CG) models can simplify spatial representations of systems and reduce the



DOI: 10.1021/acsnano.8b09741
ACS Nano 2019, 13, 4455−4468

computational cost of simulating the self-assembly of hundreds or even thousands of FF-based molecules.[22,26,28,29,49] However, most of these models neglect atomic details of peptide molecules and oftentimes cannot be used to study the conformations of peptide building blocks.

In this study, a hybrid-resolution model (termed PACE) was employed to simulate peptide self-assembly. In PACE, solvent representation is simplified using the MARTINI CG model[51] while retaining most of atomic details of proteins.[52] The PACE model has been successfully applied to obtain mechanistic insight into protein folding,[53] protein aggregation,[54] and protein−peptide interaction.[55] Here, the model has been improved for simulating the assembly of FF-based systems. The improved model allows for long-time simulation of hundreds or even thousands of FF molecules while at the same time capturing important details such as hydrogen bonds (HBs) and peptide conformations.

With this approach, we investigate the self-assembly mechanism of charged-termini-capped FFs. The N-terminally acetylated and C-terminally amidated FFs comprise two repeating peptide units and structurally resemble typical polypeptides more than the uncapped FFs. As the capped FFs can also self-assemble into nanotubes,[7,56] this FF derivative (hereinafter referred to as FF instead) was used here as a model system for conformational study of peptide self-assembly.

Extensive simulations enabled by PACE allowed us to observe the spontaneous assembly of FFs into doubled-layered patch structures that would further curve up into hollow vesicles and tubes, corroborating what was proposed previously based on CG simulations.[14,26,28] However, our simulations revealed extensive details of FF conformations that have not been observed thus far. Although there are numerous conformations accessible to FFs in water, only a select few are geometrically compatible with the assembled structures. In particular, the crystal-like conformation, which is rarely observed in water, became the dominant form in the assemblies, permitting a highly ordered packing of FFs that is energetically favorable. We found that the angle between the two aromatic side chains of FFs is a key geometric parameter associated with assembled morphologies, whereas the orientation of the backbone HB donors and receptors instead are correlated with the local packing of FFs. Although the conformations with a larger side-chain angle are not preferred in hollow vesicles or tubes, they still need to arise transiently in order to facilitate the formation of vesicles and tubes during the assembly process. These findings provide additional understanding of the relationship between conformational complexity of FFs and their self-assembly behavior, aiding to furnish guidance for the design of FF-based materials.

## RESULTS AND DISCUSSION

**Parameterization of PACE for Diphenylalanine Self-Assembly.** Previous representation of FFs with PACE captures important structural features of peptide molecules such as the packing of side chains, directionality of HBs, and the secondary structures of the backbone (Figure 1a and Figure S1 in the Supporting Information). Although this representation has permitted the application of PACE in systems like protein folding and protein−protein interactions, here, we fine-tuned the parameters of PACE to further increase its accuracy in modeling the FF self-assembly. More specifically, the parameters associated with several types of noncovalent interactions were adjusted to fit the all-atom simulation results of the FF assembly system (see Methods and Table S1). As this system contains eight FFs, it is small enough for equilibrium sampling through replica exchange molecular dynamics (REMD) simulations.[57]

In parameter fitting, focus was made on a few structural properties. The first such property was the intermolecular HB contacts between FFs, with the HB interactions involved with individual peptide bonds considered separately for the fitting. A second property was the aromatic−aromatic contacts involved with each aromatic side chain, and the third property was the spatial distributions of different parts of FFs with respect to the centers of the assembled structures. We found that where a particular part of a FF would stay in an assembly is sensitive to the balance between its interactions with other solutes and with solvent. Figure 1b−d shows these properties calculated with PACE before and after the optimization, clearly indicating that the optimized PACE had been improved.

Because it is important to test if the parameters optimized for a small FF system can be transferred to large systems, we performed simulations for two large systems (one with 810 FFs and the other with 2000 FFs). The detailed results of these simulations will be discussed later. The ability of the improved PACE to reproduce the critical concentration ($C_s$) of self-assembly of FFs was of greater interest here, as this quantity denotes the concentration at which soluble FFs reach an equilibrium with FFs in large aggregates and represents one of the most important thermodynamic parameters of aggregation.

We compared the critical concentration of FFs derived from our simulations and experiments. Computationally, the critical concentration of FFs was determined by counting the average number of dissociated FFs observed in microsecond-long simulations (Figure 1e). The calculated critical concentrations of the two FF systems tested were similar, both within a range of 0.15−0.3 mg/mL. In addition, following previous studies,[19] we also experimentally established the critical concentration of FFs by monitoring the dependence of concentration of soluble FFs as a function of total FF concentration (see Methods). As shown in Figure 1f, the peak absorption originating from the free FFs leveled off after a steady rise, indicating a $C_s$ of 0.23 mg/mL for the FFs. The good agreement of $C_s$ between both the experiments and our simulations of the two systems with different sizes (810 FFs and 2000 FFs) suggests that the improved PACE may be applicable for larger FF systems.

**Diphenylalanine Self-Assembles into Vesicles and Tubes with Double-Layered Structures.** Multiple self-assembly simulations were conducted with the improved PACE, starting with 810 randomly dispersed FFs (Tables 1 and S2). A repeating simulated annealing procedure was employed to ensure that thermodynamically stable structures were sampled, as well (see Methods).

In all the simulations, we observed the assembly of FFs into double-layered structures with a thickness of 1.4 nm with the backbones of FFs constituting the surfaces of the double-layered structures and the side chains buried inside. This

**Table 1. Observed Assembled Morphologies in Simulated Annealing Simulations of 810 FFs**

| concentration (mg/mL) | total number of MD runs | vesicle-like | tubular | sheet |
|---|---|---|---|---|
| 107 | 5 | 3 | 1 | 1 |
| 173 | 5 | 0 | 4 | 1 |



DOI: 10.1021/acsnano.8b09741
ACS Nano 2019, 13, 4455−4468

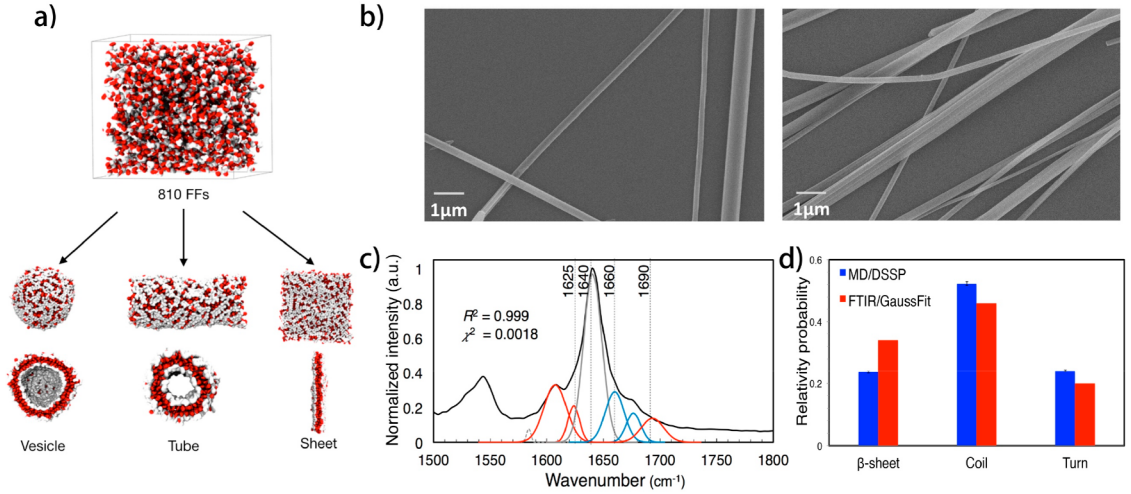


**Figure 2.** (a) Representative assembly structures observed from annealing simulations. The backbones and side chains of FFs are shown as white and red ellipsoids, respectively. (b) SEM images of FF assemblies. (c) Normalized FTIR spectrum of FF assemblies at 1500−1800 $cm^{-1}$ (black curve). The results of the Gaussian fitting are shown as red ($\beta$-sheet), blue (turn), and gray peaks (coil). The coefficients ($\chi^2$ and $R^2$) of the fitting are also shown. (d) Secondary structural contents of FF assemblies calculated from simulations (blue) and experiment (red).

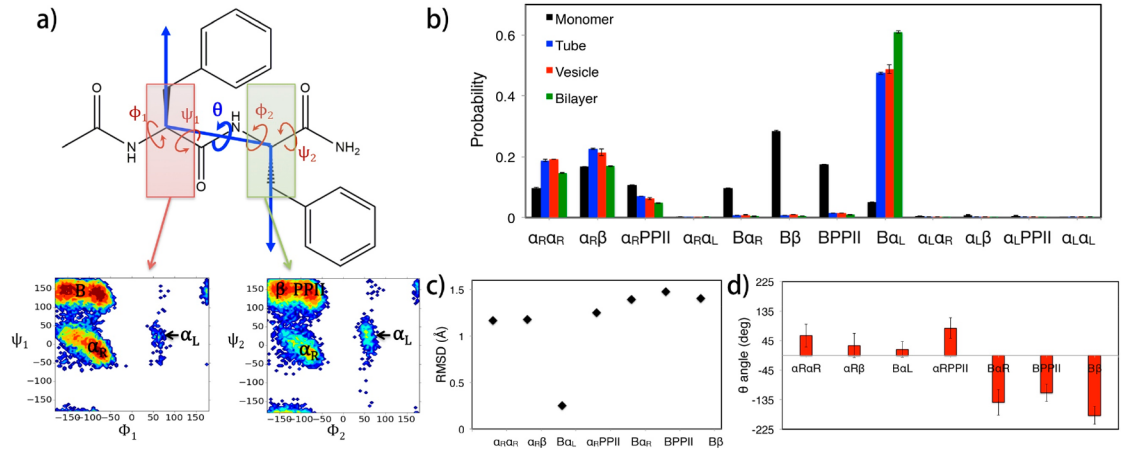


**Figure 3.** (a) Illustration of conformations of each amino acid of a FF. The Ramachandran plots were obtained from a simulation of a FF in water using PACE. (b) Conformational distributions of the FF in water (black) and in double-layered assemblies with tubular (blue), vesicular (red), and sheet-like (green) morphologies. (c) Root mean square deviations (RMSD) of representative capped FF structures to that of crystallized uncapped FFs. The RMSDs were calculated based on the overlapping backbone atoms of the capped and uncapped FFs and their $C_\beta$ atoms. (d) Angle $\theta$ of the major FF conformations. All error bars were obtained using three independent simulations.

supramolecular structure was reminiscent of a lipid bilayer. Similar assembled structures have also been reported previously in several CG simulations for uncapped FFs.[14,26,28]

At a FF concentration of 107 mg/mL, the double-layered structures primarily rolled up into hollow vesicles, and at a higher concentration (173 mg/mL), hollow tubes became dominant, extending infinitely in one dimension due to the periodic boundary conditions. At both concentrations, extended 2D sheets were occasionally observed (Figure 2a). This phenomenon, where morphology is concentration-dependent, is largely in line with previous CG simulations and experimentations.[14,26,58]

Previous scanning electron and transmission electron microscopy (SEM/TEM) studies indicate that capped FFs in water mainly assemble into long hollow nanotubes.[7,56] Our SEM measurement showed very similar assembled structures to the previous experimental observations (Figure 2b), and thus the results from the assembly simulations of 810 FFs agree qualitatively with the experimental studies. Of note, the tubes found in both previous experiments and ours were ∼100 nm up to several microns in diameter and were much wider than observed (∼6−7 nm) in the simulations (Figure S2). In addition, the tubes and vesicles observed experimentally usually have thick walls that likely involve multilaminar structures.[14,56] The smaller size of the tubes observed in the simulations could be attributed to far fewer FFs in simulations than needed for the formation of tubes with sizes comparable to what were observed in experiments. Therefore, more FFs may need to be included in simulations in order to capture large tubular structures. Indeed, as will be shown later, a microsecond-long simulation of FF self-assembly for a bigger system that contains 2000 FFs allowed us to observe a tube-like structure with a larger diameter (∼10 nm, Figure S2). However, the number of FFs needed for simulations of realistic tube structures observed experimentally is currently prohib-



DOI: 10.1021/acsnano.8b09741
ACS Nano 2019, 13, 4455−4468

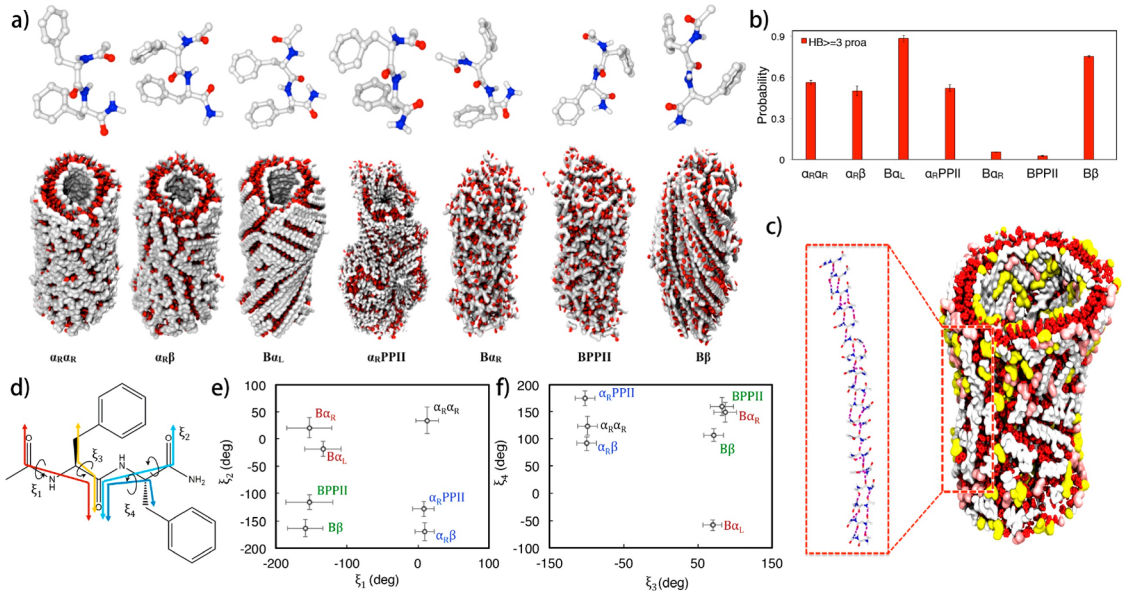


**Figure 4. (a) Representative structures of the major FF conformations (top) and corresponding assembled supramolecular structures (bottom) when FFs were constrained to each of these conformations during self-assembly simulations. The backbones and side chains of FFs are shown as white and red ellipsoids, respectively. (b) Probability of finding FFs involved in continuous HB chains when FFs were fixed to different conformations. A chain is formed through repeated parallel stacking of at least three FFs (see Supporting Information). (c) Representative tubular structure from an unconstrained simulation. FFs in $\alpha_R\alpha_R$, $\alpha_R\beta$, or $B\alpha_L$ are colored yellow, pink, or white, respectively. Inset is a close-up view of one of the HB chains. (d) Definition of $\xi_1$, $\xi_2$, $\xi_3$, and $\xi_4$. Shown in panels (e,f) are the ($\xi_1$, $\xi_2$) and ($\xi_3$, $\xi_4$) plots of the major FF conformational states. The circles denote the representative structures of the conformational states. Error bars show the standard deviation of structures that belong to each conformational state. The conformational states that are close to each other in the ($\xi_1$, $\xi_2$) map are marked in the same color. No two conformational states are close to each other in both plots except for B$\beta$ and BPPII.**

itive. This challenge is also common for many other simulation studies.[23,28,50]

We used Fourier transform infrared (FTIR) spectroscopy to analyze secondary structures of the FF assemblies to further validate the simulation results. The measured spectra exhibited strong absorption at 1500−1580 and 1600−1700 $cm^{-1}$, corresponding to amide II and I regions associated with C═O vibrations, respectively. The absorption band in the amide I region mainly was centered at ∼1641 $cm^{-1}$ while also showing considerable absorption at 1620−1640, 1660−1685, and ∼1690 $cm^{-1}$, indicating a coexistence of several types of secondary structures including coils, $\beta$-sheets, and $\beta$-turns.[59,60] Following a recent study of secondary structure characterization of short peptide assemblies,[61] we assessed fractions of different types of secondary structures by fitting the amide I band to multiple Gaussian distributions (see Figure 2c and Supporting Information). The fitting indicated that the coils are the dominant structural type, but there are still ∼34 and ∼20% chances to observe $\beta$-sheet and $\beta$-turns, respectively. We then calculated secondary structural contents from our simulations of the assembled structures formed by 810 FFs, which agreed well with those from the FTIR measurements (Figure 2d). This suggests that, despite the limitations mentioned above, the self-assembled structures in our simulations may still provide a reasonable model for identifying conformational details of FF assemblies.

**FFs Display Different Conformational Preference in Water and in Assemblies.** Next, we analyzed the conformational features of FFs in the self-assembled structures and compared these features with those found in soluble states. In the conformational analysis, all observed FF conformations were categorized into 12 different conformational states (see Table S3 and Supporting Information). Each conformational state of a FF was defined by the backbone conformational states of the two amino acid residues of the FF. The backbone conformational states of an amino acid residue represented free energy minima in the Ramachandran map of backbone dihedrals ($\phi$, $\psi$), typically including a right-handed ($\alpha_R$) and a left-handed $\alpha$-helical minima ($\alpha_L$), along with a shallow minimum (B) comprising a $\beta$-strand substate and a polyproline II substate (PPII) separated by a small free energy barrier (Figure 3a).[62] We assigned a different name to each of the conformational states of the FF. For example, when the first and the second residues of a FF are in the $\alpha_R$ and $\beta$ minima, respectively, the conformation of the FF was named $\alpha_R\beta$.

We first examined conformational features of soluble states of FFs by performing a 2 $\mu$s simulation of a single FF in water. Our simulation indicated that the conformation of a FF in water is rather diverse, with seven of the 12 conformational states having a non-negligible probability (∼5−30%). The most favorable conformation was an extended $\beta$-strand (B$\beta$) conformation, which is consistent with the high tendency of phenylalanine to adopt a $\beta$ conformation.[63] To confirm this finding, we also conducted conformational analyses on structures of FF segments taken from a coil library in the protein data bank (PDB) (see Supporting Information). PDB coil libraries have been proven to be accurate in characterizing intrinsic conformational propensities of amino acids,[64−66] and as shown in Figure S3, there is good agreement between the conformational distribution of FFs obtained from our soluble-state simulation and those from the coil library. This finding also demonstrated the ability of PACE to describe conformations of soluble FFs.

Figure 3b shows the conformational distributions of FFs in various double-layered assemblies, which include vesicles, tubes, and sheets. These assembly structures were obtained



DOI: 10.1021/acsnano.8b09741
ACS Nano 2019, 13, 4455−4468

from the self-assembly simulations of 810 FFs mentioned earlier. The conformational preferences of FFs in these assemblies are similar regardless of their morphologies, and the comparison with the data from the simulation of a free FF demonstrated a marked difference between the conformational distributions of FFs in water and in the assemblies. In particular, three major conformational states (B$\alpha_R$, B$\beta$, and BPPII) accessible to soluble FFs rarely formed in the assembled structures, whereas the B$\alpha_L$ conformer that was scarcely populated (~5%) in water became the predominant conformation (>50−60%) in the assembled structures. Interestingly, this conformation was very similar to the crystal structure of uncapped FFs. The root-mean-square distance (RMSD) between the representative structure of B$\alpha_L$ and the crystal structure was ~0.2 Å and was much lower than the RMSD values (>1.1 Å) obtained for the other conformations. This result supports the previous assumption that FFs adopt the crystal-like conformation in aqueous assemblies (Figure 3c).[8,25,43,44,67]

**Molecular Basis of Conformational Preference of FFs in Self-Assembled Structures.** The results above suggest that assembled structures of FFs are conformationally specific, and to understand the molecular basis of this conformational specificity better, we performed a series of conformationally constrained simulations of 810 FFs in which constraints were applied to maintain all the FFs in the system in single conformational states (see Methods). This approach provides a useful means by which to investigate the correlation between a given FF conformation and assembled structures under idealized circumstances. The conformational states examined were those with an intrinsic probability greater than 5% (Figure 3b).

The constrained simulations clearly indicated that the FFs constrained to different conformations could self-assemble into nanostructures with distinct morphologies (Figure 4a). We analyzed the geometric features of FF conformations to provide insight into the relationship between each FF conformation and its corresponding assembled morphology. We first examined the angle $\theta$ between the two side chains of a FF, a key geometric parameter of FFs that has been previously demonstrated.[23,28,43] When $\theta$ is small (closer to 0°), the two side chains are positioned on the same side of peptide backbone (called a *syn* arrangement); when $\theta$ is large (closer to 180°), the two side chains are positioned on the opposite sides of the backbone (called an *anti* arrangement).

Our analysis revealed that when FFs were constrained to the conformations B$\alpha_L$, $\alpha_R\alpha_R$, or $\alpha_R\beta$, double-layered structures such as hollow tubes were formed (Figures 4a and S4). All three of these conformations exhibited small $\theta$ ($|\theta| < 60°$, Figure 3d), and when the FFs were fixed to $\alpha_R$PPII whose $\theta$ was a right angle, we observed the formation of irregular porous assemblies containing ring-shape substructures. For B$\alpha_L$, B$\beta$, and BPPII that had large $\theta$ angles ($|\theta| > 115°$), the constrained simulations always gave rise to aggregates in spherical or rod-like shapes. These aggregates lacked any large internal hollow chambers as were also seen in the double-layered assemblies (Figure 2a). Of note, a very thin tunnel with a diameter of 1−1.5 nm was observed in the elongated aggregates formed by FFs when fixed to a B$\beta$ conformation (Figure S5). Collectively, these findings suggest that a correlation exists between the side-chain arrangement of FFs and assembled morphologies.

Aside from the overall morphologies, the packing of FFs in the assemblies observed in the constrained simulations was also investigated. Different patterns of molecular packing were observed in the same types of assembled morphologies (either double-layered assemblies or aggregates) depending on the conformational states of FF building blocks (Figures 4a and S4). Highly ordered packing of FFs in the double-layered assemblies and the aggregates was observed only when FFs were constrained to B$\alpha_L$ or B$\beta$, respectively, and involved repeated parallel stacking of FFs that allowed continuous HB chain structures to form. There is a considerably lower probability of the involvement of the other conformational states in the HB chain structures (Figure 4b).

It would be helpful to understand what geometric features of FFs could be responsible for such diversity of molecular packing in the assembled structures. As the major forces driving molecular packing of FFs include aromatic attraction between side chains and HB interactions between backbone, the correlation between the observed packing patterns and the geometric features pertaining to these interaction types was investigated. We first examined the relative arrangement of the two side chains of FFs as it could affect how the FFs form aromatic contacts with their nearest neighbors. However, because the conformations compatible with the same type of assembled morphology exhibit a similar side-chain arrangement, this geometric factor alone cannot explain the observed difference in patterns of FF packing. Therefore, we focused instead on the geometric features pertaining to intermolecular HB interactions. Specifically, we analyzed the relative orientation of backbone HB donors and acceptors that were described by the angles ($\xi_1$ and $\xi_2$, shown in Figure 4d) between the three peptide bonds of a FF and those ($\xi_3$ and $\xi_4$) between the side chains and the central peptide bond. The internal orientation distribution of HB donors and acceptors of FFs can affect their coordination propensities, and the analysis revealed a large variation in $\xi$ among the different conformations. No two conformations exhibited similar values ($|\Delta\xi| < 90°$) in all $\xi$ angles except for B$\beta$ and BPPII (Figure 4e,f). This large variation in the orientation of HB donors and acceptors may have accounted for the diversity observed for the FF packing in the assemblies.

The insights derived from the ideal constrained simulations helped us in understanding the results of the more realistic unconstrained simulations for the 810 FF systems. The three conformational states, including B$\alpha_L$, $\alpha_R\alpha_R$, and $\alpha_R\beta$, that were predicted by the constrained simulations compatible with the double-layered structures were also conformations that were frequently observed (with a chance >15%) in the unconstrained simulations (Figure 3b). The other conformations that were predicted to be favored in aggregates, such as B$\beta$, B$\alpha_R$, and BPPII, had a negligible chance (<1%) to occur in the unconstrained simulations.

In addition, the results from the constrained simulations also aided in explaining why the crystal-like conformation (particularly, B$\alpha_L$) was more favorable than $\alpha_R\alpha_R$ and $\alpha_R\beta$ for the double-layered assemblies (Figure 3b). The constrained simulations allowed us to analyze the degree of stabilization the assemblies would gain if FFs predominantly adopted a particular conformation state. Our analyses covered several types of stabilizing forces that were regarded previously as crucial for peptide assembly, including interpeptide HB, aromatic interactions, and interactions between solvent and the FF backbone.[25,48,49] FFs adopting B$\alpha_L$ consistently



DOI: 10.1021/acsnano.8b09741
ACS Nano 2019, 13, 4455−4468

provided 5−10% more stabilization to the double-layered assemblies than they did when adopting $\alpha_R\alpha_R$ or $\alpha_R\beta$ for all interaction types examined (Table 2). This additional stability renders B$\alpha_L$ more favorable than $\alpha_R\alpha_R$ and $\alpha_R\beta$ in the double-layered assemblies, even though B$\alpha_L$ is much less populated in water.

**Table 2. Noncovalent Contacts Formed in the Assembled Structures Observed in Conformationally Constrained Simulations**[a]

| | backbone/water | side chain/side chain | HB |
|---|---|---|---|
| $\alpha_R\alpha_R$ | 5.5 ± 0.1 | 160 ± 2 | 1.52 ± 0.01 |
| $\alpha_R\beta$ | 6.8 ± 0.1 | 158.2 ± 0.2 | 1.47 ± 0.01 |
| B$\alpha_L$ | 7.4 ± 0.2 | 168.4 ± 0.2 | 1.69 ± 0.03 |

[a]All the contacts were averaged over all FFs. Two particles were thought to form a contact if they are closer than 0.4 nm.

According to the constrained simulations, when FFs adopts B$\alpha_L$, the doubled-layered structures with continuous HB chain structures would arise, and because B$\alpha_L$ was determined to be the most abundant conformation in the unconstrained simulations, one would expect that the HB chains would be prevalent structural features of the doubled-layered assemblies. The representative structure of the double-layered assemblies taken from the unconstrained simulations indeed showed that there are many HB chain structures mainly formed by the FFs in the B$\alpha_L$ conformation (Figure 4c).

**Conformational Transitions during the Self-Assembly of FFs.** The conformational difference between soluble and assembled FFs observed in the present study corroborates the suggestion that there is a large conformational transition of FFs during the self-assembly process.[39] In order to gain insight into the nature by which this transition takes place, we conducted an unbiased simulation of FF self-assembly. As suggested by a previous simulation study,[28] although simulations of hundreds of FFs are efficient in sampling basic nanostructures assembled by FFs, large simulation systems containing several thousand FFs may often be needed for more realistic modeling of complex processes of FF self-assembly. As such, our unbiased simulation included 2000 FFs in a box with a size of 30 × 30 × 30 nm$^3$, and the length of the simulation reached 2.2 $\mu$s.

Shortly after the simulation started ($t$ = ∼10 ns), the FFs that were initially dispersed had quickly assembled into small clusters containing 20−30 monomers (Figure 5a,b). During the next 150 ns of simulation, these small clusters associated into small double-layered patches (at $t$ = ∼50−100 ns) that continued to merge into several large patches. The two largest patches then curved up into vesicles, and the two resulting vesicles collided at $t$ = ∼500 ns, eventually fusing into a capsule. Although a tubular structure was not observed, the cylindrical part of the capsule displayed a morphology very similar to the tubular assemblies that had been observed in our annealing simulations (Figure 2a). As this capsule would have continued to grow into a tube if it absorbed more vesicles, our results agree with the previous suggestion that the FF tubes may result from the fusion of vesicles.[11,14,58]

We monitored the change in probability of the major conformational states of FFs during the assembly process of 2000 FFs. The probabilities of detecting B$\beta$, B$\alpha_R$, and BPPII (as shown in Figure 5c,d) diminished rapidly within the first

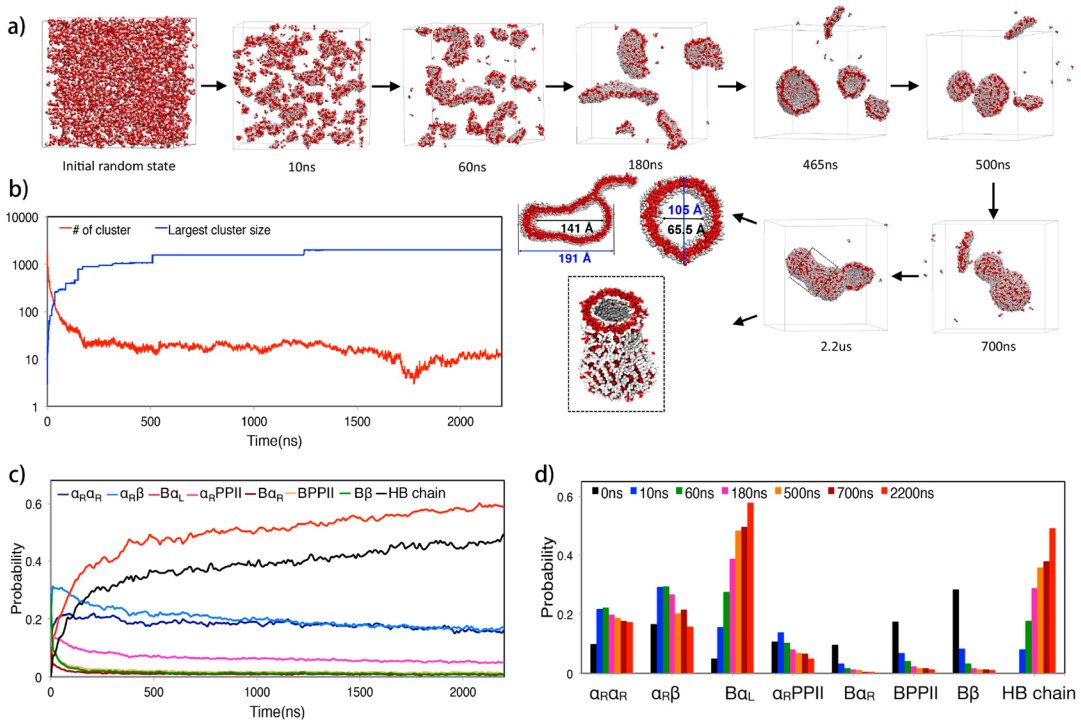


**Figure 5. (a) Snapshots taken from self-assembly simulation of 2000 FFs. (b) Time evolution of the number of clusters (red curves) and the number of FFs contained in the largest cluster (blue lines) during the simulation. A group of FFs was thought to form a cluster if any of these FFs has at least one atomic contact with the others. Two atoms were thought to contact each other if their distance is shorter than 0.45 nm. (c) Time evolution of conformational distribution of FFs and probability of finding a FF in HB chains during the simulation. (d) Conformational distribution of FFs and probability of finding HB chains at select time points of the assembly simulation.**



DOI: 10.1021/acsnano.8b09741
ACS Nano 2019, 13, 4455−4468

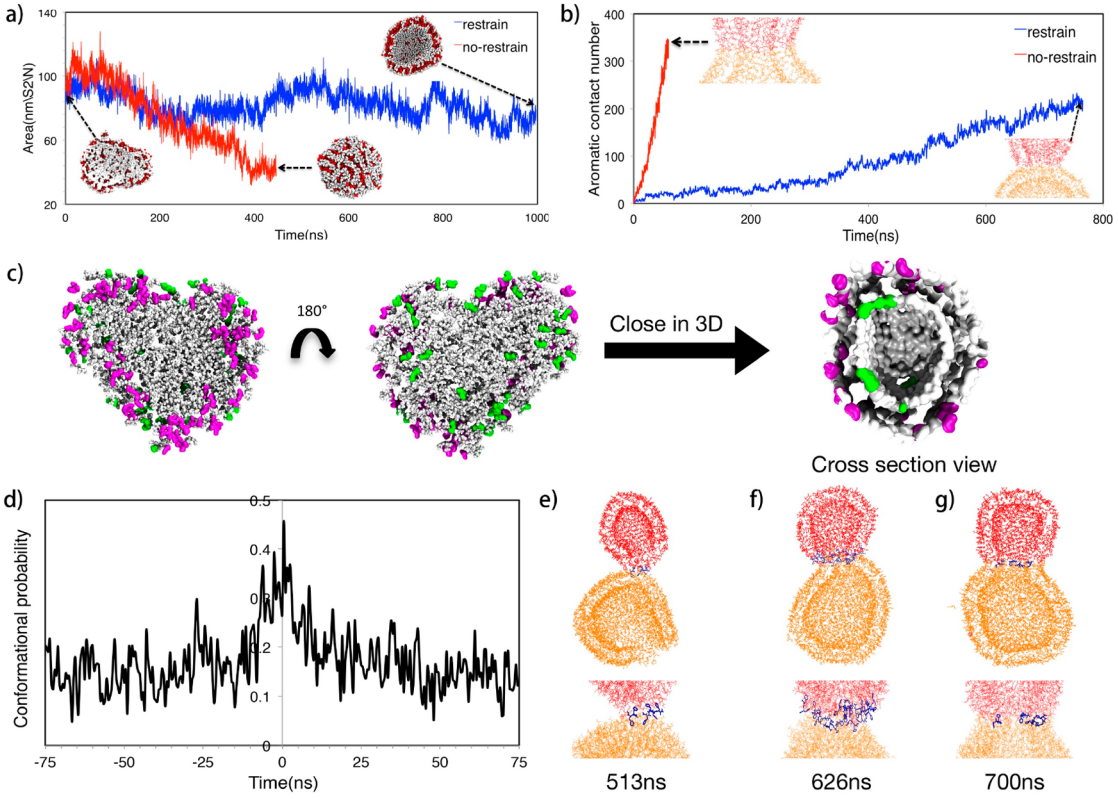


**Figure 6. Simulation tests of impact of conformational fluctuation on closure of the double-layered patches (a) and fusion of vesicles (b). Blue and red curves denote the results from the simulations with and without conformational constraints, respectively. The simulations of patch closure and vesicle fusions began with a patch containing ∼500 FFs and two vesicles containing in total ∼1500 FFs, respectively. Shown in (a) is the time evolution of total accessible surface areas of side chains which mainly arose from the exposed edges of the patch. Shown in (b) is the time evolution of aromatic contacts formed between aromatic rings from different vesicles (colored red and orange, respectively). (c) Repartitioning of FFs between the two leaflets of a double-layered patch during the closure of the patch. The patch and the vesicle evolved from the patch were taken from the simulation of 2000 FFs at $t$ = 180 ns and $t$ = 510 ns, respectively. The FFs in each leaflet that traversed the double-layered structure are marked purple and green, respectively. (d) Probability of finding FFs in B$\beta$, B$\alpha_R$, BPPII, and $\alpha_R$PPII during their traverse movement across the double-layered structure. The results were averaged over the trajectories of all the FFs that had traversed the double-layered structures. The time zero corresponds to the moment that a FF was positioned between the two leaflets during its traverse movement. (e−g) Snapshots during fusion of two vesicles taken from the 2000 FF system. The two vesicles are colored red and orange, respectively. Marked blue are the FFs that form aromatic contacts with both vesicles while adopting one of B$\beta$, B$\alpha_R$, BPPII, and $\alpha_R$PPII conformations.**

50−100 ns of the simulation and remained negligible beyond this time period. Conversely, the probabilities of $\alpha_R\alpha_R$, $\alpha_R\beta$, and $\alpha_R$PPII rapidly increased at the beginning of the simulation and then peaked early ($t$ = ∼50−100 ns), gradually decreasing until the end of the simulation. For B$\alpha$L, its probability quickly increased initially and then continued to increase more slowly throughout the remaining simulation. At the early stage of the assembly, it seems that FFs rapidly redistributed their conformational states to eliminate the conformations with large $\theta$ and instead populate those with small $\theta$. This conformational transition appears necessary for initial formation of small clusters and double-layered patches. At the later stages of the assembly, a slow conformational convention took place, shifting the population toward the B$\alpha_L$ conformation. As the majority of free FFs had already been absorbed after the initial stages of the assembly, the conformational changes afterward occurred within the aggregates. This means that the aggregated environment did not suppress the conformational transitions of FFs, and our analysis of state-to-state transition over the second half of the simulation of 2000 FFs indeed revealed that the transition times between different FF conformations in the assemblies was at most ∼10 ns (Figure S6). These transitions were much faster compared to the assembly process.

The probability of observing FFs in B$\alpha_L$ throughout the simulation was closely correlated with the probability of observing FFs involved in the continuous HB chain structures (Figure 5c,d). This result corroborates our hypothesis that B$\alpha_L$ is needed for FFs to provide ordered intermolecular packing in the double-layered assemblies, therefore indicating that the conformational conversion of FFs into B$\alpha_L$ could be an important type of conformational transition that leads to the ordered packing of FFs.

**Importance of Transient Conformational Change for Self-Assembly of FFs.** Our simulation of self-assembly of 2000 FFs revealed that, even in aggregates, there were rapid conformational fluctuations of FFs that were responsible for the conversion of FFs from soluble to assembled states. We performed a series of conformationally constrained simulations to determine how the dynamics of several key steps of the self-assembly process might be affected by the suppression of conformational fluctuations of FFs. The steps examined included the initial formation of double-layered patches, the



DOI: 10.1021/acsnano.8b09741
ACS Nano 2019, 13, 4455−4468

closure of the patches into vesicles, and the fusion of the vesicles into capsules.

Specifically, we performed multiple test simulations containing randomly dispersed FFs to examine the assembly dynamics of flat patch structures formed at the initial stage of the assembly process. According to the simulation of 2000 FF, this type of patch structure normally contained about 100 FFs at least. Hence, 100 FFs were included in these test simulations. In half of the test simulations, the conformations of FFs were constrained in such a way that the resulting conformational distribution was consistent with that obtained at the time point ($t$ = 200 ns) of the simulation of 2000 FFs when the patches had already occurred (see Methods). In the other half of the test simulations, no such constraints were applied. In all of the simulations, we observed the formation of a small double-layered patch at $t$ = ∼100 ns (Figure S7), indicating that the conformation fluctuation of FFs is not essential for the formation of these patch structures.

After the assembly dynamics of small patches, we then examined the closure of the double-layered patches. The test simulations began with a flat patch containing ∼500 FFs taken from a frame at $t$ = 180 ns of the simulation of 2000 FFs. As done previously, these simulations were performed in the absence or in the presence of conformational constraints, and in the constrained test simulations, each FF was constrained to its starting conformation. In the constraint-free test simulations, vesicles formed within 350 ns, as indicated by a large reduction in the solvent accessible surface area of aromatic side chains that were exposed at the patch edges. In contrast, the patches in the 1 $\mu$s constrained simulations were far from being closed, leaving a large number of aromatic side chains exposed at the patch edges (Figures 6a and S8), indicating that the suppression of the conformational fluctuation of FFs impeded vesicle closure.

Similarly, our test simulations of vesicle fusion began with a system containing two vesicles that were about to form initial contact. The coordinates of the system (containing ∼1500 FFs) were taken from a frame of $t$ = 502 ns of the simulation of 2000 FFs, and the fusion event usually occurred within the first 200 ns of the unconstrained test simulations, but never took place during the 600−800 ns constrained simulations (Figures 6b and S9). At the end of the constrained test simulations, the two vesicles partly shared their walls at best but by no means joined together to form a connected internal chamber and thus indicated that the conformational fluctuation of FFs is also important for the process of vesicle fusion.

We sought to understand further the importance of the conformational fluctuation of FFs to the formation and fusion of vesicles. As the double-layered patches had conformational distributions of FFs very similar to those of the vesicles (Figure 3b), it was supposed that there would be little need for FFs to change their conformational distribution when the patches curved into vesicles. Despite this, we noticed that the partition of FFs between the two leaflets of the double-layered structures was different for the patches and vesicles. For instance, the large flat patches observed in our 2000 FF simulation contained almost equal numbers of FFs in each of their two leaflets (Table S4), and once they turned into vesicles, the outer leaflets of the vesicles contained 100−150 more FFs than their inner leaflets (probably due to the smaller surface area of the inner leaflet of a vesicle being able to accommodate fewer FFs). Based on this information, the transformation of the patches to the vesicles must involve a redistribution of FFs for both leaflets.

The simulation of 2000 FFs also allowed us to trace the movement of every single FF during the formation of vesicles, and we found that tens of FFs in the inner leaflet of the vesicle actually came from the edge part of the patch leaflet that had eventually evolved into the outer leaflet of the vesicle (Table S4 and Figure 6c). Conversely, twice as many FFs in the outer leaflet of the vesicles came from the edge part of the other leaflet from the flat patches. This finding indicates that the repartitioning of FFs between the two leaflets of the patches was mainly achieved by the flip-flop of FFs in the patches.

We then examined why the conformational fluctuation of FFs was important for the flip-flop of these molecules. We calculated a time series of the conformational states during the vesicle formation for each FF involved in flip-flop, and all the resulting time series were aligned such that their time origins coincide to when the FFs happened to be located between the two leaflets. These aligned time series provided a statistical description of conformational change associated with the flip-flop of FFs.

As shown in Figure 6d, the population of the conformations with large $\theta$ increased transiently (from 10−15% to 45−50%) and peaked half way during the flip-flop of the FFs even though the conformations with small $\theta$ were dominant conformations of FFs in the double-layered structures. This finding suggests that a transient conformational transition of FFs to those with large $\theta$ seemed crucial for the flip-flop of FFs and, subsequently, for the transformation of the patches into the vesicles.

Additionally, we identified all the FFs adopting this type of conformation during the fusion process in the interfacial regions of the two vesicles (Figures 6e−g) to test if a similar transient conversion of FFs may also be needed for the fusion process. Again, the results from the simulation of 2000 FFs were used for the analysis. Upon the initial contacts of the two vesicles, most of FFs at the interface needed to assume the conformations with a larger $\theta$ (Figure 6e) because a FF in these conformations can keep one of its side chains in the vesicle where the FF originally stayed while inserting its other side chain into a second vesicle. At the middle and late stages of the fusion process, there was also a largely increased chance to observe the FFs assuming the large $\theta$ conformations in the junction region of the two vesicles (Figure 6f), but once the fusion process ended, the chance to observe the large $\theta$ conformations in this region diminished (Figure 6g). Based on these findings, a transient conversion of FFs into the conformations with large $\theta$ is most likely essential at various stages of the vesicle fusion process.

## CONCLUSIONS

The rational design of self-assembled materials relies on a deep understanding of the relationship between the building block structures and resulting assembled structures. In this study, we explored through extensive simulations the conformational complexity of diphenylalanine molecules and elucidated upon the influences of the conformational complexity regarding both morphologies and molecular packing associated with assembled structures as well as assembly dynamics.

Our simulations demonstrated that there are numerous conformations accessible to FFs that exhibit diverse molecular geometries. The conformations involving a *syn* arrangement of the two aromatic side chains best fit in double-layered



DOI: 10.1021/acsnano.8b09741
ACS Nano 2019, 13, 4455−4468

structures that can further roll up into hollow vesicles and tubes similar to those observed experimentally. Although a similar role of this type of side chain arrangement has also been reported by others,[23,28,43] we showed that the FFs with a large angle between the side chains tended to assemble into ordered or partially ordered aggregates lacking in any of the large internal cavities that was normally observed in the double-layered assemblies. Although these types of aggregates have not been reported for FF assemblies in water, they are attainable in other solvent environment.[33,68] Additionally, a previous SEM/TEM study showed that a FF derivative conformationally locked by chemical modification into an *anti* arrangement of side chains could assemble into thin linear assemblies in water. Unlike those hollow assemblies formed by unmodified FFs, these assembled structures exhibited very thin tunnels (with diameters <2 nm) at best.[35] A similar morphology was observed in our assembly simulations when FFs were constrained to one of the conformations with large side-chain angles (Figures S5), which may represent an atomic model for the assemblies that were observed experimentally. Collectively, our study reveals the critical role of side-chain arrangement in determining assembled morphologies.

Furthermore, we have identified other geometric factors aside from the side chain arrangement that also can affect molecular architectures of the assemblies. Although multiple conformations that share the similar side chain arrangement are compatible with assemblies with similar morphology (either doubled-layered assemblies or aggregates), they usually differ from one other in terms of geometric details like the relative orientation of backbone HB donors and acceptors. As a result, the packing of FFs in the assemblies can be conformationally specific, and only a select few conformations permit a highly ordered packing of FFs in the assemblies. These results shed light on the intricate dependencies of molecular architecture of assemblies on multiple FF geometric factors and highlight the need in considering the full conformational details of peptide building blocks in their molecular design.

Although the FF conformation obtained from crystal has been widely accepted as a model for FF conformation in assemblies,[25,43,44,67] its relevance to these assemblies (which are formed in a fully hydrated environment) remains ambiguous.[17,45,46] To date, all-atom simulation studies have failed to observe the conformation during the self-assembly of small systems containing tens of FFs in water.[25,48,49] Our simulations demonstrate that this conformation, although unstable in isolation or in small clusters of FFs, can be gradually enriched and eventually become dominant during the spontaneous assembly of many FFs into double-layered assemblies like hollow vesicles and tubes. When compared to the other conformations, the special geometry of this conformation allows FFs to pack into assemblies in an energetically favorable, highly ordered manner. Therefore, our results provide compelling evidence that supports the relevance of the crystal conformation to the assembled hollow tubes and vesicles.

It has been supposed that the dynamics of internal conformations of protein-like building blocks play crucial roles in the assembly mechanism,[40,69] with possible roles of the conformational fluctuations having been probed computationally at CG level for several other assembly systems.[41,42] In the study presented here, our computational investigation of atomic details of FF assembly revealed at least two possible roles of conformational fluctuations in the self-assembly of FFs: (1) the fulfillment of the conformational transformation of FFs from disordered monomer states into ordered aggregation states, which basically reiterates what was concluded in those CG studies,[41,42] and (2) the transient conversion of FFs into particular intermediate conformations that are required for the closure of double-layered patches into vesicles and fusion of vesicles into tubes. The observed intermediate conformations usually displayed large side-chain angles, which does not match the structures that were assembled eventually. Although the significance of this transient conformational conversion needs to be confirmed by further experimentation, a similar phenomenon has already been reported in several cases of peptide aggregation during which the transient formation of helical structures was discovered to expedite the formation of amyloid fibrils rich in $\beta$-sheets.[70,71]

Our simulations explain the molecular rationale behind the role played by these intermediate conformations further. During the transformation from a flat patch to a vesicle, a double-layered structure must create an imbalance of FFs between its two leaflets achieved mainly through the flip-flop of FFs in the patch with large side-chain angle conformations. Intriguingly, it was found in previous simulation work that lipid molecules needed to open up their two tails when traversing bilayer membrane.[72] During the fusion of two vesicles, the FFs in the interfacial region also tended to adopt similar conformations in order to facilitate the initial attachment of the vesicles along with the subsequent opening of vesicle walls. This molecular explanation adds a crucial layer of mechanistic details of the self-assembly of FFs and would be helpful for understanding self-assembly of protein-like molecules in general.

We were able to observe the atomic details of the self-assembly process of hundreds and even thousands of peptide molecules into experimentally observed nanostructures using the hybrid-resolution model presented in this study. When combined with conformationally constrained simulations, the model can further be utilized into assessing the conformational impact on the assembly process and can predict possible assembled structures for conformationally restrained peptides. In conclusion, this hybrid-resolution model shows potential as a valuable computational tool for studying the self-assembly of peptide-based molecules like FFs and providing aid in the design of related materials.

## METHODS

**Peptide Synthesis.** Peptide synthesis was performed manually on Rink amide MBHA resin (loading capacity: 0.54 mmol/g) (GL Biochem Co. Ltd.) by standard Fmoc-based solid-phase peptide synthesis. Generally, Rink amide AM resin was preswelled with DCM/NMP (1/1) for 30 min. Fmoc deprotection was performed with morpholine (50% in NMP) for 30 min × 2. Then the resin was washed with NMP (5 times), DCM (5 times), and NMP (5 times). Fmoc-protected amino acids (6.0 equiv according to initial loading of the resin) and HCTU (5.9 equiv) were dissolved in NMP, followed by DIPEA (12.0 equiv). The mixture was preactivated for 1 min and added to the resin for 1−2 h, then the resin was washed with NMP (5 times), DCM (5 times), and NMP (5 times). Upon completion of peptide synthesis, peptides were N-terminally acetylated with a solution of acetic anhydride and DIPEA in NMP (1:1:8 in volume) for 1 h. Peptides were cleaved from the resin with a mixture of TFA/$H_2O$/EDT/TIS (94:2.5:2.5:1) for 2 h and concentrated under a stream of nitrogen. The crude peptides were then precipitated with



DOI: 10.1021/acsnano.8b09741
*ACS Nano* 2019, 13, 4455−4468

hexane/$Et_2O$ (1:1 in volume) at −20 °C, isolated by centrifugation, then dissolved in water/acetonitrile, purified by semipreparative HPLC, and analyzed by LC-MS.

**Preparation.** Fresh peptide stock solution was prepared by dissolving lyophilized dipeptide powder in 1,1,1,3,3,3-hexafluoro-2-propanol (HFIP, Sigma) at a concentration of 100 mg/mL. The stock solutions were then diluted to a desired concentration in deionized water.

**Scanning Electron Microscopy.** Immediately after dilution in deionized water (final concentration of 0.5 mg/mL), peptide solution was placed on silicon slides, left to dry at room temperature, and coated with gold. Samples were then viewed using a scanning electron microscope (ZEISS Supra 55, Oxford X-Max 20, 20 kV).

**Fourier Transform Infrared Spectroscopy.** Peptide solution was taken from SEM assay and dried by vacuum. KBr pellet was prepared prior to measurement. Qualitative analysis of the samples was performed. A Bruker Vertex 70 FTIR spectrometer was used for FTIR analysis with wavenumber range from 4000 to 400 $cm^{-1}$.

**Critical Concentration.** Critical concentration was measured at 258 nm at 330 K, using a molar absorption coefficient of 390 $M^{-1}$ $cm^{-1}$, calculated from the molar absorption coefficient of phenylalanine. To explore the potential subcritical association in deionized water, solutions at concentrations of 0.05−0.80 mg/mL were prepared. These were incubated for 1 h and then ultracentrifuged for 1 h at 62000*g*. The supernatant was measured, and the absorption at 258 nm was plotted against concentration.

**Parameterization of the PACE Model.** The potential energy function of PACE is expressed as

$$E = E_{\text{bond}} + E_{\text{angle}} + E_{\text{dihedral}} + E_{\text{improper}} + E_{\phi,\psi,\chi 1} + E_{\text{CGW-CGW}} + E_{\text{CGW-UA}} + E_{\text{nonpolar}} + E_{\text{polar}} \quad (1)$$

where the first five terms describe the bonded energy and geometry and rotameric preference in proteins and the last four terms describe noncovalent interactions between protein sites, between CG water sites and between the two types of sites at different resolutions. These energy terms and their parametrization have been thoroughly explained in our previous studies and the Supporting Information.[53,73]

In this study, the noncovalent parameters of PACE (version 1.3) were further fine-tuned to fit the results from simulations of eight FFs using the CHARMM27 force field[74] and the TIP3P solvent model[75] that has been validated for studying protein and peptide self-assembly systems.[48,76] Specifically, we adjusted the parameters for HB interaction strength, described as the well depth of Lennard-Jones potential between HB donor and acceptor atoms, to reproduce HB patterns formed between FFs (Figure S1 and Table S1). In addition, we also adjusted the parameters associated with the interaction between peptide sites and CG water to correctly model aromatic−aromatic contacts and the distance-to-center distributions. We conducted an iterative trial-and-error procedure to optimize these parameters against the all-atom results while attempting to minimize change made to PACE. The optimized parameters are listed in Table 3. Of note, despite these changes, PACE can still be used to simulate *ab initio* folding of the mini-protein systems (Figure S10) that were employed previously to validate PACE.[53] This suggests that the changes made to the force field, though important for correct modeling of self-assembly, are fairly small and do not affect simulation results at a single molecular level.

**Table 3. Parameters Adjusted for Self-Assembly Simulations in This Study**[a]

| interaction type | N−O | HA−O | CZ−W | CA−W | C−W |
|---|---|---|---|---|---|
| original PACE | 17.7 | 20 | 0.81 | 1.15 | 0.8 |
| optimized PACE | 17.2 | 18.82 | 0.926 | 0.805 | 0.56 |

[a]All parameters adjusted are those associated with well depth ($\varepsilon$, in unit of kJ $mol^{-1}$) of LJ potentials describing nonbonded interactions between several pairs of atom types, namely, N, O, HA, and C for amide nitrogen, oxygen, hydrogen, and carbon, respectively, CA for $C_\alpha$ of backbone, CZ for carbon atoms in aromatic rings, and W for coarse-grained water particles.

**Models and Simulation Setup.** All simulations in this study were conducted using the GROMACS 4.5.4 package.[77] In all-atom systems, either a single FF or eight FFs were placed in a cubic box containing 1181 and 1026 TIP3P water molecules, respectively. The particle mesh Ewald[78] method was employed to calculate electrostatic interactions with a short-range cutoff of 1.2 nm. The REMD simulations were performed with 16 replicas at temperatures of 289−405 K. Temperature in simulations was kept using the Nosé−Hoover method. Simulation time step was 2 fs with the LINCS algorithm. Exchange between replicas was attempted every 10 ps with average acceptance ratio of >20%. The total simulation length was 750 ns for the monomer system and 3.2 $\mu$s for the octamer system. The data collected at 310 K were used for the fitting.

The simulation setup for each system modeled with PACE is summarized in Table S2. In general, a number of FFs were initially randomly dispersed in a simulation box with a clearance of 0.5 nm. The MARTINI CG water was used to solvate the systems. All the systems were subject to a 5000 step energy minimization followed by a 5 ns pre-equilibration at 310 K with system volume being fixed. Then production runs were conducted at 1 atm. The Nosé−Hoover method and the Parrinello−Rahman method were used to maintain simulation temperature and pressure, respectively.

For simulated annealing simulations, the following temperature scheme was adopted. The systems were first maintained at the highest temperature for 50−200 ns and then cooled at a speed of 0.5 K/ns. The systems stayed at the lowest temperature for 20 ns before another annealing cycle starts over. Typically, two to five annealing cycles were conducted for each simulation, followed by a long time equilibrium run at 330 K that was employed for analysis.

In conformationally constrained simulations, each FF was constrained to one of the 12 possible conformational states *via* harmonic forces applied to $\phi_1$, $\psi_1$, $\phi_2$, and $\psi_2$ of the backbone of the FF. The force constants and the equilibrium values of the harmonic forces were optimized against the results of the unconstrained self-assembly simulations (Figure S11). These parameters are listed in Table S5.

## ASSOCIATED CONTENT

### Supporting Information

The Supporting Information is available free of charge on the ACS Publications website at DOI: 10.1021/acsnano.8b09741.

Tables S1−5, Figures S1−S11, and detailed descriptions of PACE force field and structural analysis methods (PDF)

## AUTHOR INFORMATION


### Corresponding Authors

*E-mail: lizg@pkusz.edu.cn.
*E-mail: hanw@pkusz.edu.cn.

### ORCID

Zigang Li: 0000-0002-3630-8520
Wei Han: 0000-0003-0759-1766


### Author Contributions

†Q.X. and Y.J. contributed equally to this work.

### Notes

The authors declare no competing financial interest.

## ACKNOWLEDGMENTS

We thank the National Science Foundation of China (21673013 to W.H. and 21778009 to Z.G.L.) and the Shenzhen STIC (KQTD2015032709315529 to W.H., JCYJ20160330095839867 to W.H., JCYJ20170818085409785 to W.H., and JCYJ20170412150719814 to Z.G.L.) for financial



DOI: 10.1021/acsnano.8b09741
*ACS Nano* 2019, 13, 4455−4468

support. The computational work is supported by the High-Performance Computing Platform of Peking University.

## REFERENCES

(1) Kim, S.; Kim, J. H.; Lee, J. S.; Park, C. B. Beta-Sheet-Forming, Self-Assembled Peptide Nanomaterials towards Optical, Energy, and Healthcare Applications. *Small* **2015**, *11*, 3623−3640.
(2) Adler-Abramovich, L.; Gazit, E. The Physical Properties of Supramolecular Peptide Assemblies: from Building Block Association to Technological Applications. *Chem. Soc. Rev.* **2014**, *43*, 6881−6893.
(3) Tao, K.; Makam, P.; Aizen, R.; Gazit, E. Self-Assembling Peptide Semiconductors. *Science* **2017**, *358*, No. eaam9756.
(4) Tao, K.; Levin, A.; Adler-Abramovich, L.; Gazit, E. Fmoc-Modified Amino Acids and Short Peptides: Simple Bio-Inspired Building Blocks for The Fabrication of Functional Materials. *Chem. Soc. Rev.* **2016**, *45*, 3935−3953.
(5) Lee, O. S.; Stupp, S. I.; Schatz, G. C. Atomistic Molecular Dynamics Simulations of Peptide Amphiphile Self-Assembly into Cylindrical Nanofibers. *J. Am. Chem. Soc.* **2011**, *133*, 3677−3683.
(6) Reches, M.; Gazit, E. Casting Metal Nanowires within Discrete Self-Assembled Peptide Nanotubes. *Science* **2003**, *300*, 625−627.
(7) Reches, M.; Gazit, E. Self-Assembly of Peptide Nanotubes and Amyloid-Like Structures by Charged-Termini-Capped Diphenylalanine Peptide Analogues. *Isr. J. Chem.* **2005**, *45*, 363−371.
(8) Li, Q.; Jia, Y.; Dai, L.; Yang, Y.; Li, J. Controlled Rod Nanostructured Assembly of Diphenylalanine and Their Optical Waveguide Properties. *ACS Nano* **2015**, *9*, 2689−2695.
(9) Levin, A.; Mason, T. O.; Adler-Abramovich, L.; Buell, A. K.; Meisl, G.; Galvagnion, C.; Bram, Y.; Stratford, S. A.; Dobson, C. M.; Knowles, T. P.; Gazit, E. Ostwald's Rule of Stages Governs Structural Transitions and Morphology of Dipeptide Supramolecular Polymers. *Nat. Commun.* **2014**, *5*, 5219.
(10) Smith, A. M.; Williams, R. J.; Tang, C.; Coppo, P.; Collins, R. F.; Turner, M. L.; Saiani, A.; Ulijn, R. V. Fmoc-Diphenylalanine Self Assembles to a Hydrogel *via* a Novel Architecture Based on $\pi-\pi$ Interlocked $\beta$-Sheets. *Adv. Mater.* **2008**, *20*, 37−41.
(11) Yan, X.; He, Q.; Wang, K.; Duan, L.; Cui, Y.; Li, J. Transition of Cationic Dipeptide Nanotubes into Vesicles and Oligonucleotide Delivery. *Angew. Chem.* **2007**, *119*, 2483−2486.
(12) Reches, M.; Gazit, E. Formation of Closed-Cage Nanostructures by Self-Assembly of Aromatic Dipeptides. *Nano Lett.* **2004**, *4*, 581−585.
(13) Ryu, J.; Park, C. B. High Stability of Self-Assembled Peptide Nanowires Against Thermal, Chemical, and Proteolytic Attacks. *Biotechnol. Bioeng.* **2010**, *105*, 221−230.
(14) Song, Y.; Challa, S. R.; Medforth, C. J.; Qiu, Y.; Watt, R. K.; Pena, D.; Miller, J. E.; van Swol, F.; Shelnutt, J. A. Synthesis of Peptide- Nanotube Platinum-Nanoparticle Composites. *Chem. Commun.* **2004**, *9*, 1044−1045.
(15) Kol, N.; Adler-Abramovich, L.; Barlam, D.; Shneck, R. Z.; Gazit, E.; Rousso, I. Self-Assembled Peptide Nanotubes are Uniquely Rigid Bioinspired Supramolecular Structures. *Nano Lett.* **2005**, *5*, 1343−1346.
(16) Yan, X.; Zhu, P.; Li, J. Self-Assembly and Application of Diphenylalanine-Based Nanostructures. *Chem. Soc. Rev.* **2010**, *39*, 1877−1890.
(17) Frederix, P. W. J. M.; Patmanidis, I.; Marrink, S. J. Molecular Simulations of Self-Assembling Bio-Inspired Supramolecular Systems and Their Connection to Experiments. *Chem. Soc. Rev.* **2018**, *47*, 3470−3489.
(18) Lampel, A.; Ulijn, R. V.; Tuttle, T. Guiding Principles for Peptide Nanotechnology through Directed Discovery. *Chem. Soc. Rev.* **2018**, *47*, 3737−3758.
(19) Mason, T. O.; Michaels, T. C. T.; Levin, A.; Dobson, C. M.; Gazit, E.; Knowles, T. P. J.; Buell, A. K. Thermodynamics of Polypeptide Supramolecular Assembly in the Short-Chain Limit. *J. Am. Chem. Soc.* **2017**, *139*, 16134−16142.
(20) Reddy, S. M. M.; Shanmugam, G. Role of Intramolecular Aromatic p−p Interactions in the Self-Assembly of Di-l-Phenylalanine Dipeptide Driven by Intermolecular Interactions: Effect of Alanine Substitution. *ChemPhysChem* **2016**, *17*, 2897−2907.
(21) Mishra, A.; Chauhan, V. S. Probing the Role of Aromaticity in the Design of Dipeptide Based Nanostructures. *Nanoscale* **2011**, *3*, 945−949.
(22) Brown, N.; Lei, J.; Zhan, C.; Shimon, L. J. W.; Adler-Abramovich, L.; Wei, G.; Gazit, E. Structural Polymorphism in a Self-Assembled Tri-Aromatic Peptide System. *ACS Nano* **2018**, *12*, 3253−3262.
(23) Guo, C.; Luo, Y.; Zhou, R.; Wei, G. Triphenylalanine Peptides Self-Assemble into Nanospheres and Nanorods That Are Different from the Nanovesicles and Nanotubes Formed by Diphenylalanine Peptides. *Nanoscale* **2014**, *6*, 2800−2811.
(24) Rissanou, A. N.; Georgilis, E.; Kasotakis, E.; Mitraki, A.; Harmandaris, V. Effect of Solvent on the Self-Assembly of Dialanine and Diphenylalanine Peptides. *J. Phys. Chem. B* **2013**, *117*, 3962−3975.
(25) Jeon, J.; Mills, C. E.; Shell, M. S. Molecular Insights into Diphenylalanine Nanotube Assembly: All-Atom Simulations of Oligomerization. *J. Phys. Chem. B* **2013**, *117*, 3935−3943.
(26) Guo, C.; Luo, Y.; Zhou, R.; Wei, G. Probing the Self-Assembly Mechanism of Diphenylalanine-Based Peptide Nanovesicles and Nanotubes. *ACS Nano* **2012**, *6*, 3907−3918.
(27) Wang, J.; Liu, K.; Xing, R.; Yan, X. Peptide Self-Assembly: Thermodynamics and Kinetics. *Chem. Soc. Rev.* **2016**, *45*, 5589−5604.
(28) Frederix, P. W. J. M.; Ulijn, R. V.; Hunt, N. T.; Tuttle, T. Virtual Screening for Dipeptide Aggregation: Toward Predictive Tools for Peptide Self-Assembly. *J. Phys. Chem. Lett.* **2011**, *2*, 2380−2384.
(29) Frederix, P. W. J. M.; Scott, G. G.; Abul-Haija, Y. M.; Kalafatovic, D.; Pappas, C. G.; Javid, N.; Hunt, N. T.; Ulijn, R. V.; Tuttle, T. Exploring the Sequence Space for (Tri-)Peptide Self-Assembly to Design and Discover New Hydrogels. *Nat. Chem.* **2015**, *7*, 30−37.
(30) Hamley, I. W. Peptide Nanotubes. *Angew. Chem., Int. Ed.* **2014**, *53*, 6866−6881.
(31) Dinesh, B.; Squillaci, M. A.; Menard-Moyon, C.; Samori, P.; Bianco, A. Self-Assembly of Diphenylalanine Backbone Homologues and Their Combination with Functionalized Carbon Nanotubes. *Nanoscale* **2015**, *7*, 15873−15879.
(32) Xing, R.; Yuan, C.; Li, S.; Song, J.; Li, J.; Yan, X. Charge-Induced Secondary Structure Transformation of Amyloid-Derived Dipeptide Assemblies from Beta-Sheet to Alpha-Helix. *Angew. Chem., Int. Ed.* **2018**, *57*, 1537−1542.
(33) Zhu, P.; Yan, X.; Su, Y.; Yang, Y.; Li, J. Solvent-Induced Structural Transition of Self-Assembled Dipeptide: From Organogels to Microcrystals. *Chem. - Eur. J.* **2010**, *16*, 3176−3183.
(34) Erdogan, H.; Babur, E.; Yilmaz, M.; Candas, E.; Gordesel, M.; Dede, Y.; Oren, E. E.; Demirel, G. B.; Ozturk, M. K.; Yavuz, M. S.; Demirel, G. Morphological Versatility in the Self-Assembly of Val-Ala and Ala-Val Dipeptides. *Langmuir* **2015**, *31*, 7337−7345.
(35) Gupta, M.; Bagaria, A.; Mishra, A.; Mathur, P.; Basu, A.; Ramakumar, S.; Chauhan, V. S. Self-Assembly of a Dipeptide-Containing Conformationally Restricted Dehydrophenylalanine Residue to Form Ordered Nanotubes. *Adv. Mater.* **2007**, *19*, 858−861.
(36) Amdursky, N.; Molotskii, M.; Gazit, E.; Rosenman, G. Elementary Building Blocks of Self-Assembled Peptide Nanotubes. *J. Am. Chem. Soc.* **2010**, *132*, 15632−15636.
(37) Edison, J. R.; Spencer, R. K.; Butterfoss, G. L.; Hudson, B. C.; Hochbaum, A. I.; Paravastu, A. K.; Zuckermann, R. N.; Whitelam, S. Conformations of Peptoids in Nanosheets Result from the Interplay of Backbone Energetics and Intermolecular Interactions. *Proc. Natl. Acad. Sci. U. S. A.* **2018**, *115*, 5647−5651.
(38) Johny, M.; Vijayalakshmi, K.; Das, A.; Roy, P.; Mishra, A.; Dasgupta, J. Modulating the Phe-Phe Dipeptide Aggregation Landscape *via* Covalent Attachment of an Azobenzene Photoswitch. *Chem. Commun.* **2017**, *53*, 9348−9351.
(39) Ishikawa, M. S.; Busch, C.; Motzkus, M.; Martinho, H.; Buckup, T. Two-Step Kinetic Model of the Self-Assembly Mechanism



DOI: 10.1021/acsnano.8b09741
*ACS Nano* 2019, 13, 4455−4468

for Diphenylalanine Micro/Nanotube Formation. *Phys. Chem. Chem. Phys.* **2017**, *19*, 31647−31654.
(40) Whitelam, S.; Jack, R. L. The Statistical Mechanics of Dynamic Pathways to Self-Assembly. *Annu. Rev. Phys. Chem.* **2015**, *66*, 143−163.
(41) Nguyen, T. D.; Glotzer, S. C. Reconfigurable Assemblies of Shape-Changing Nanorods. *ACS Nano* **2010**, *4*, 2585−2594.
(42) Whitelam, S.; Rogers, C.; Pasqua, A.; Paavola, C.; Trent, J.; Geissler, P. L. The Impact of Conformational Fluctuations on Self-Assembly: Cooperative Aggregation of Archaeal Chaperonin Proteins. *Nano Lett.* **2009**, *9*, 292−297.
(43) Görbitz, C. H. Nanotube Formation by Hydrophobic Dipeptides. *Chem. - Eur. J.* **2001**, *7*, 5153−5159.
(44) Görbitz, C. H. The Structure of Nanotubes Formed by Diphenylalanine, the Core Recognition Motif of Alzheimer's $\beta$-amyloid Polypeptide. *Chem. Commun.* **2006**, *22*, 2332−2334.
(45) Houton, K. A.; Morris, K. L.; Chen, L.; Schmidtmann, M.; Jones, J. T. A.; Serpell, L. C.; Lloyd, G. O.; Adams, D. J. On Crystal *versus* Fiber Formation in Dipeptide Hydrogelator Systems. *Langmuir* **2012**, *28*, 9797−9806.
(46) Adams, D. J.; Morris, K.; Chen, L.; Serpell, L. C.; Bacsa, J.; Day, G. M. The Delicate Balance between Gelation and Crystallisation: Structural and Computational Investigations. *Soft Matter* **2010**, *6*, 4144−4156.
(47) Lampel, A.; McPhee, S. A.; Park, H.-A.; Scott, G. G.; Humagain, S.; Hekstra, D. R.; Yoo, B.; Frederix, P. W. J. M.; Li, T.-D.; Abzalimov, R. R.; Greenbaum, S. G.; Tuttle, T.; Hu, C.; Bettinger, C. J.; Ulijn, R. V. Polymeric Peptide Pigments with Sequence-Encoded Properties. *Science* **2017**, *356*, 1064−1068.
(48) Tamamis, P.; Adler-Abramovich, L.; Reches, M.; Marshall, K.; Sikorski, P.; Serpell, L.; Gazit, E.; Archontis, G. Self-Assembly of Phenylalanine Oligopeptides: Insights from Experiments and Simulations. *Biophys. J.* **2009**, *96*, 5020−5029.
(49) Guo, C.; Arnon, Z. A.; Qi, R.; Zhang, Q.; Adler-Abramovich, L.; Gazit, E.; Wei, G. Expanding the Nanoarchitectural Diversity Through Aromatic Di- and Tri-Peptide Coassembly: Nanostructures and Molecular Mechanisms. *ACS Nano* **2016**, *10*, 8316−8324.
(50) Mishra, A.; Chauhan, V. S. Probing the Role of Aromaticity in the Design of Dipeptide Based Nanostructures. *Nanoscale* **2011**, *3*, 945−949.
(51) Marrink, S. J.; Risselada, H. J.; Yefimov, S.; Tieleman, D. P.; de Vries, A. H. The MARTINI Force Field: Coarse Grained Model for Biomolecular Simulations. *J. Phys. Chem. B* **2007**, *111*, 7812−7824.
(52) Han, W.; Wan, C.; Jiang, F.; Wu, Y. PACE Force Field for Protein Simulations. 1. Full Parameterization of Version 1 and Verification. *J. Chem. Theory Comput.* **2010**, *6*, 3373−3389.
(53) Han, W.; Schulten, K. Further Optimization of a Hybrid United-Atom and Coarse-Grained Force Field for Folding Simulations: Improved Backbone Hydration and Interactions between Charged Side Chains. *J. Chem. Theory Comput.* **2012**, *8*, 4413−4424.
(54) Cao, Y.; Jiang, X.; Han, W. Self-Assembly Pathways of Beta-Sheet-Rich Amyloid-Beta(1−40) Dimers: Markov State Model Analysis on Millisecond Hybrid-Resolution Simulations. *J. Chem. Theory Comput.* **2017**, *13*, 5731−5744.
(55) Jiang, X.; Cao, Y.; Han, W. In Silico Study of Recognition between A$\beta$40 and Abeta40 Fibril Surfaces: An N-Terminal Helical Recognition Motif and Its Implications for Inhibitor Design. *ACS Chem. Neurosci.* **2018**, *9*, 935−944.
(56) Reches, M.; Gazit, E. Controlled Patterning of Aligned Self-Assembled Peptide Nanotubes. *Nat. Nanotechnol.* **2006**, *1*, 195−200.
(57) Hukushima, K.; Nemoto, K. Exchange Monte Carlo Method and Application to Spin Glass Simulations. *J. Phys. Soc. Jpn.* **1996**, *65*, 1604−1608.
(58) Yan, X. H.; Cui, Y.; He, Q.; Wang, K. W.; Li, J. B.; Mu, W. H.; Wang, B.; Ou-yang, Z. C. Reversible Transitions between Peptide Nanotubes and Vesicle-Like Structures including Theoretical Modeling Studies. *Chem. - Eur. J.* **2008**, *14*, 5974−5980.
(59) Barth, A. Infrared Spectroscopy of Proteins. *Biochim. Biophys. Acta, Bioenerg.* **2007**, *1767*, 1073−1101.
(60) Jackson, M.; Mantsch, H. H. The Use and Misuse of FTIR Spectroscopy in the Determination of Protein Structure. *Crit. Rev. Biochem. Mol. Biol.* **1995**, *30*, 95−120.
(61) Seo, J.; Hoffmann, W.; Warnke, S.; Huang, X.; Gewinner, S.; Schollkopf, W.; Bowers, M. T.; von Helden, G.; Pagel, K. An Infrared Spectroscopy Approach to Follow Beta-Sheet Formation in Peptide Amyloid Assemblies. *Nat. Chem.* **2016**, *9*, 39−44.
(62) Pizzanelli, S.; Forte, C.; Monti, S.; Zandomeneghi, G.; Hagarman, A.; Measey, T. J.; Schweitzer-Stenner, R. Conformations of Phenylalanine in the Tripeptides AFA and GFG Probed by Combining MD Simulations with NMR, FTIR, Polarized Raman, and VCD Spectroscopy. *J. Phys. Chem. B* **2010**, *114*, 3965−3978.
(63) Grdadolnik, J.; Mohacek-Grosev, V.; Baldwin, R. L.; Avbelj, F. Populations of the Three Major Backbone Conformations in 19 Amino Acid Dipeptides. *Proc. Natl. Acad. Sci. U. S. A.* **2011**, *108*, 1794−1798.
(64) Jiang, F.; Han, W.; Wu, Y. D. The Intrinsic Conformational Features of Amino Acids from a Protein Coil Library and Their Applications in Force Field Development. *Phys. Chem. Chem. Phys.* **2013**, *15*, 3413−3428.
(65) Fitzkee, N. C.; Fleming, P. J.; Rose, G. D. The Protein Coil Library: A Structural Database of Nonhelix, Nonstrand Fragments Derived from the PDB. *Proteins: Struct., Funct., Genet.* **2005**, *58*, 852−854.
(66) Perskie, L. L.; Street, T. O.; Rose, G. D. Structures, Basins, and Energies: A Deconstruction of the Protein Coil Library. *Protein Sci.* **2008**, *17*, 1151−1161.
(67) Yan, X.; Li, J.; Mohwald, H. Self-Assembly of Hexagonal Peptide Microtubes and Their Optical Waveguiding. *Adv. Mater.* **2011**, *23*, 2796−2801.
(68) Wang, J.; Liu, K.; Yan, L.; Wang, A.; Bai, S.; Yan, X. Trace Solvent As a Predominant Factor To Tune Dipeptide Self-Assembly. *ACS Nano* **2016**, *10*, 2138−2143.
(69) Lee, E.; Kim, J.; Lee, M. Reversible Scrolling of Two-Dimensional Sheets from the Self-Assembly of Laterally Grafted Amphiphilic Rods. *Angew. Chem., Int. Ed.* **2009**, *48*, 3657−3660.
(70) Misra, P.; Kodali, R.; Chemuru, S.; Kar, K.; Wetzel, R. Rapid $\alpha$-Oligomer Formation Mediated by the Abeta C Terminus Initiates an Amyloid Assembly Pathway. *Nat. Commun.* **2016**, *7*, 12419.
(71) Hauser, C. A.; Deng, R.; Mishra, A.; Loo, Y.; Khoe, U.; Zhuang, F.; Cheong, D. W.; Accardo, A.; Sullivan, M. B.; Riekel, C.; Ying, J. Y.; Hauser, U. A. Natural Tri- to Hexapeptides Self-Assemble in Water to Amyloid Beta-Type Fiber Aggregates by Unexpected Alpha-Helical Intermediate Structures. *Proc. Natl. Acad. Sci. U. S. A.* **2011**, *108*, 1361−1366.
(72) Song, B.; Yuan, H.; Pham, S. V.; Jameson, C. J.; Murad, S. Nanoparticle Permeation Induces Water Penetration, Ion Transport, and Lipid Flip-Flop. *Langmuir* **2012**, *28*, 16989−17000.
(73) Han, W.; Wan, C.; Wu, Y. PACE Force Field for Protein Simulations. 2. Folding Simulations of Peptides. *J. Chem. Theory Comput.* **2010**, *6*, 3390−3402.
(74) MacKerell, A. D., Jr; Feig, M.; Brooks, C. L., 3rd. Extending the Treatment of Backbone Energetics in Protein Force Fields: Limitations of Gas-Phase Quantum Mechanics in Reproducing Protein Conformational Distributions in Molecular Dynamics Simulations. *J. Comput. Chem.* **2004**, *25*, 1400−1415.
(75) Jorgensen, W. L.; Chandrasekhar, J.; Madura, J. D.; Impey, R. W.; Klein, M. L. Comparison of Simple Potential Functions for Simulating Liquid Water. *J. Chem. Phys.* **1983**, *79*, 926−935.
(76) Ramos Sasselli, I.; Ulijn, R. V.; Tuttle, T. CHARMM Force Field Parameterization Protocol for Self-Assembling Peptide Amphiphiles: The Fmoc Moiety. *Phys. Chem. Chem. Phys.* **2016**, *18*, 4659−4667.
(77) Hess, B.; Kutzner, C.; van der Spoel, D.; Lindahl, E. GROMACS 4: Algorithms for Highly Efficient, Load-Balanced, and Scalable Molecular Simulation. *J. Chem. Theory Comput.* **2008**, *4*, 435−447.


DOI: 10.1021/acsnano.8b09741
*ACS Nano* 2019, 13, 4455−4468

(78) Essmann, U.; Perera, L.; Berkowitz, M. L.; Darden, T.; Lee, H.; Pedersen, L. G. A Smooth Particle Mesh Ewald Method. *J. Chem. Phys.* **1995**, *103*, 8577−8593.



DOI: 10.1021/acsnano.8b09741
*ACS Nano* 2019, 13, 4455−4468